Chapter 6
Geometric Studies of the Plasma Torch Anode

"It is the glory of geometry that from so few principles, fetched from without, it is able to accomplish so much." Isaac Newton

Plasma torches have been shown to be effective igniters and flameholders for supersonic combustion applications, both experimentally and analytically. To maximize the effectiveness of the torch as an igniter and flameholder, experimental geometric studies of flow injection angle, throat length, and nozzle areas were performed. These studies assisted in the understanding of how these parameters affect the torch performance, and shed light on how to enhance the torch as an igniter and flameholder for supersonic combustion applications.

This chapter presents data collected during a two-part geometric study of plasma torch anodes, cataloguing the effect of geometric changes on torch performance. The first part of the study involves changing the angle of the diverging section of the anode. The goal of this study was to determine if the arc needs protection from the supersonic crossflow, and if possible, remove the diverging section entirely so as to eliminate the volume inside the diverging section where plasma recombination occurs. This would maximize the effectiveness of the torch in a crossflow by allowing more of the plasma jet energy to encounter the cross-flowing fuel. Preliminary quiescent experiments were conducted to evaluate how these design changes affected the required power to operate the torch, while the subsequent protection studies were conducted in an unheated Mach 3.0 crossflow (T_t = 300 K, P_t = 379 kPa). To supplement this study, surface oil flow pictures were taken to study the dependency of the shape of the bow shock, separation zones, and plume reattachment points on the geometry of the diverging section. The experiments demonstrated that the plasma torch operates well with each of the geometries, and a diverging section was not needed to protect the arc from the supersonic crossflow. In addition, torch power requirements were actually lowest for the design with no diverging section, an added benefit.

The second phase of the geometric study was more extensive and was aimed at altering the throat-to-length ratio of the anode constrictor, altering the injection angle of the torch, and determining if a supersonic nozzle increased the penetration height of the

plasma jet. Evaluations of the designs were made using thermodynamic probing and spectroscopic analyses of the plasma jet. A spectrometer was used to measure the spectral intensity of the H_β line from the Balmer series at the torch exit for torch input powers between 1 and 4.5 kW. Excited hydrogen atoms were chosen as the specie to track, since hydrogen atoms are known to enhance combustion. Downstream temperature probes measured the total temperature of the torch plume to determine how the plume height and shape changed for various geometries and operational conditions. In addition, stereoscopic photographs of the anode surfaces were taken after the tests were complete to provide a better understanding of how geometric changes affect arc attachment and anode wear rate. Evaluation of spectral and temperature data demonstrated that anodes designed for normal injection produced higher spectral intensities within the jet, and higher total temperatures downstream of the torch, when compared to anodes designed for transverse injection. The combination of these two observations indicates a greater ignition potential. Comparisons of the anode constrictor lengths showed that longer constrictors, although producing higher jet intensities, are unstable due to the longer arc column. Finally, supersonic nozzles were found to increase the total temperature of the downstream plumes, but had poor penetration and failed to eject any plasma above the tunnel floor for powers less than 1700 W.

6.2: Test Procedure

6.2.1: Anode Exit Geometry

The tests designed to study the effect of changing the angle of the diverging section of the anode were conducted using VTPT-2 with tungsten anodes. The anodes used to study the effect of the anode diverging section on torch performance are shown in Figure 6.1. The throat length for each design was kept constant at 1.02 mm, except for the 90° case, which had a longer throat length of 2.26 mm. This difference was tolerated because it was necessary to keep the overall height of the anode the same so that the anode surface would be flush with the tunnel floor in the supersonic crossflow experiments. The operating conditions for the tests are shown in Table 6.1. Values for pressure and current were selected to produce high powers, allowing changes in torch power for different anode geometries to be more easily identified. In the quiescent

environment, power data were collected over a period of 60 seconds at a sample rate of 1000 Hz. Three of these 60-second tests were conducted for each test condition so that an average power requirement and data scatter could be determined. Experiments conducted in the supersonic tunnel used only methane as the feedstock gas, with a chamber pressure of 689 kPa to provide a momentum flux ratio of 2.0. A high-speed digital camera verified the presence of plasma in the supersonic crossflow with a framerate of 500 frames per second. Surface oil flow experiments were conducted while the torch was off, using fluorescent dye suspended in 500cB oil.

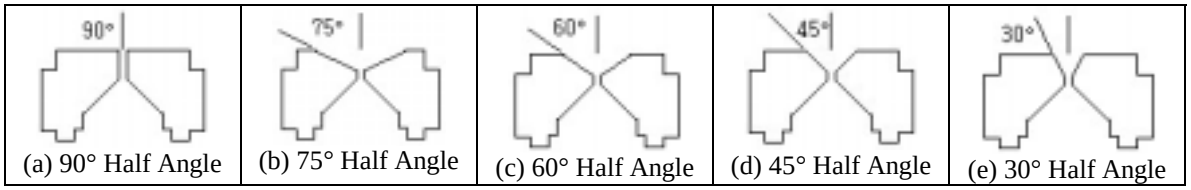

(a) 90° Half Angle (b) 75° Half Angle (c) 60° Half Angle (d) 45° Half Angle (e) 30° Half Angle

Figure 6.1: Anode Exit Geometries

Table 6.1: Operating Conditions for the Anode Angle Experiments

Feedstock Gas:	Current	Torch Chamber Pressure	Test Duration	Number of Tests
Methane (Quiescent)	24 A	513 kPa	60 sec	3 per anode
Methane (Tunnel)	24 A	689 kPa	10 sec	N/A
Argon (Quiescent)	38 A	756 kPa	60 sec	3 per anode

6.2.2: Studies of Nozzles, Throat Lengths, and Injection Angle

Diagrams of the anodes used for the second stage of the anode geometry study are shown in Figure 6.2. Six designs were tested, three 90° designs and three 60° designs, corresponding to normal and transverse injection respectively. For each angle set, there are three subsets: an anode with a 2.54 mm throat length, an anode with a 3.18 mm throat length, and an anode with a 1.78 mm throat length and a supersonic nozzle. These six designs allowed performance comparisons to be made on the basis of throat length, injection angle, and the addition of a supersonic nozzle to the anode constrictor. The 60° sonic designs were machined so that the anode face would remain flush to the tunnel floor, producing an elliptical constrictor exit and nonuniform constrictor length. As reported, the throat length is measured from the shortest portion of the anode constrictor, corresponding to the point at which arc attachment was expected. The supersonic designs have a throat length of 1.78 mm, shorter than the other two designs since the arc was

expected to attach outside of the throat. It was desired to keep the arc length of the supersonic anodes comparable to the short-throated designs. Therefore, the throat length of the supersonic design was chosen assuming the arc attached one-third the distance up the nozzle based on past experience (Gallimore, 1998). To facilitate easy discussion, these designs are referred to by their injection angle, followed by the anode geometry description, as shown in Figure 6.2. (Ex. The 60° anode with the 3.18 mm throat will be referred to as the 60°-sonic-long anode design.) Each design was tested in a Mach 2.4 crossflow, with power ranging from 1-4.5 kW and momentum flux ratios of 1.17 or 2.34.

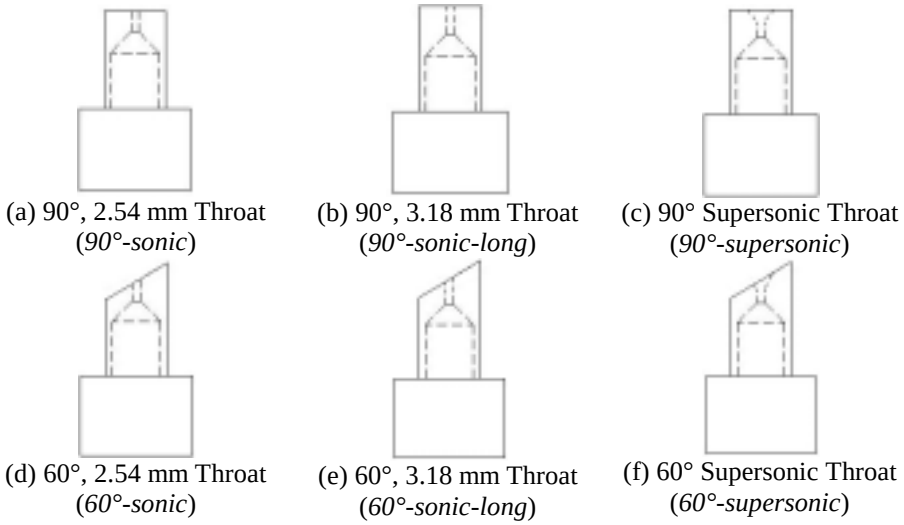

(a) 90°, 2.54 mm Throat (*90°-sonic*)
(b) 90°, 3.18 mm Throat (*90°-sonic-long*)
(c) 90° Supersonic Throat (*90°-supersonic*)
(d) 60°, 2.54 mm Throat (*60°-sonic*)
(e) 60°, 3.18 mm Throat (*60°-sonic-long*)
(f) 60° Supersonic Throat (*60°-supersonic*)

Figure 6.2: Anode Designs for the Nozzle, Throat Geometry and Injection Angle Study

6.2.3: Stereoscopic Investigation of Anode Wear

Magnified optical evaluations of the anode surfaces were made by use of a stereoscope, which could be used to take pictures of the anode surfaces. The observations made of the anode surfaces showed where the arc attachment point was located, whether or not the arc attachment point moved during operation, and how the arc changed the shape of the anode surface through erosion. This type of investigation resulted in a better understanding of the type of anode wear associated with various geometric features.

6.3: Results and Discussion

The results are presented in two separate sections, the first discussing the geometric study of the diverging section of the anode, and the second an investigation of the effects of supersonic nozzles, throat length, and injection angle on torch performance. The discussion of the second study is presented in such a way that comparisons of the six designs are presented first, followed by subsections discussing operational trends for each specific design.

6.3.1: Studies of the Anode Diverging Section

Regarding the investigations of the effect that the anode diverging section has on the operability of the torch, the main result is that the torch was observed to light in a Mach 3.0 crossflow for all anode designs (refer to Figure 6.1), even with no diverging section present to protect the arc. In addition, power requirements for anodes with constant diameter exit nozzles were generally lower than for anodes with a diverging section.

6.3.1.1: Results of the Power Requirements

As expected, experiments with argon produced smooth operation for all tests. The results were repeatable and produced power readings that fluctuated very little from the mean reported values in Figure 6.3. From the figure, it is clear that the 45° design requires the most power to operate, while the other designs require about 20% less. Since current was held constant, these power differences are due solely to the voltage requirements, which is a combined effect of both the arc length and arc shape. Analysis of the anodes after testing showed that the arc attachment point for the 45° case was slightly outside the anode throat in the diverging section, while for the 60° and 75° designs the arc attachment point was at the boundary of the throat and diverging section. From this, conclusions can be drawn that a shorter arc length caused, at least in part, the lower voltage requirements for the 60° and 75° cases. Although the 90° design has the longest anode constrictor, it experienced the lowest power of all four designs, which is quite significant. The voltage requirements for this geometry were less, because there was less arc curvature (Somerville, 1959), but also may be attributed to radius of

curvature effects on the electric field (refer to Section 4.3.4.2). Slight anode wear at the constrictor exit proved that the arc traveled the entire length of the constrictor.

Results for methane show much the same pattern. Again, the 45° anode design requires the most power to sustain the arc, with the other designs requiring 10-15% less. In this case, the 90° design is not the lowest power consumer but is still several hundred W lower than the traditional 45° design. Inspection of the anodes after testing showed similar arc attachment points as with argon, indicating the same arc shapes. Observation of the torch during testing also showed that the 90° design consistently produced a methane flame originating at the plasma jet. The other designs produced intermittent flames, except for the 60° design, which produced no flame plume whatsoever. This performance difference can be attributed to the diverging section of the anode, which essentially acts as a plasma recombination region, and hence, reduces the amount of available energy to initiate combustion once the methane mixes with the surrounding air.

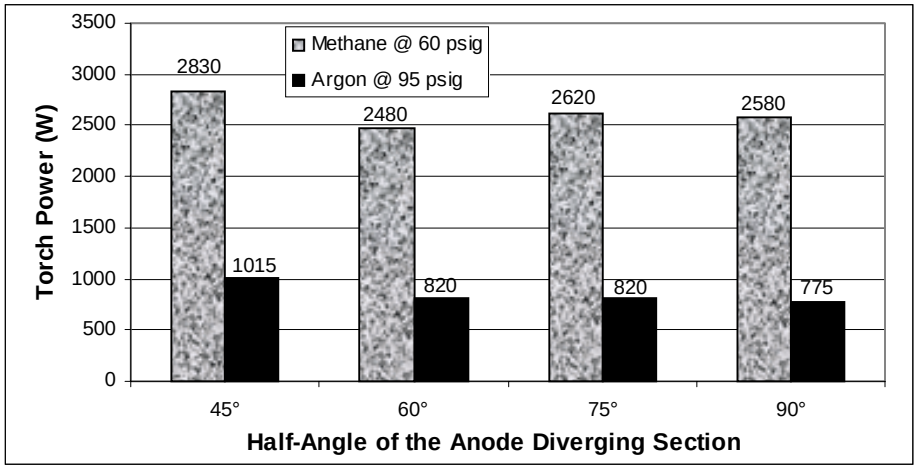

Figure 6.3: Power Relationships for Different Anode Half Angles

6.3.1.2: Results of the Protection Studies

Tests in a Mach 3.0 crossflow showed that an arc could be sustained with each of the five anode designs and a diverging section was not needed to protect the arc. A high-speed digital camera captured the dynamics of the plasma jet as the torch operated in the supersonic crossflow. Time averages of these pictures are shown in Figure 6.4, where eight pictures taken at the same point in the voltage cycle have been averaged to present the general shape of the plasma jet for each geometry. The direction of flow is from left to right. The plasma jet produced by the 90° design is the smallest, with the other designs

being larger to varying degrees. However, the smaller size of the plasma jet does not necessarily imply lower ignition potential since the energy density of the plasma jets could not be determined with these techniques. Furthermore, the plasma jet produced by the 90° design penetrates slightly further than the other designs, a desirable characteristic for igniting cross-flowing fuel-air mixtures.

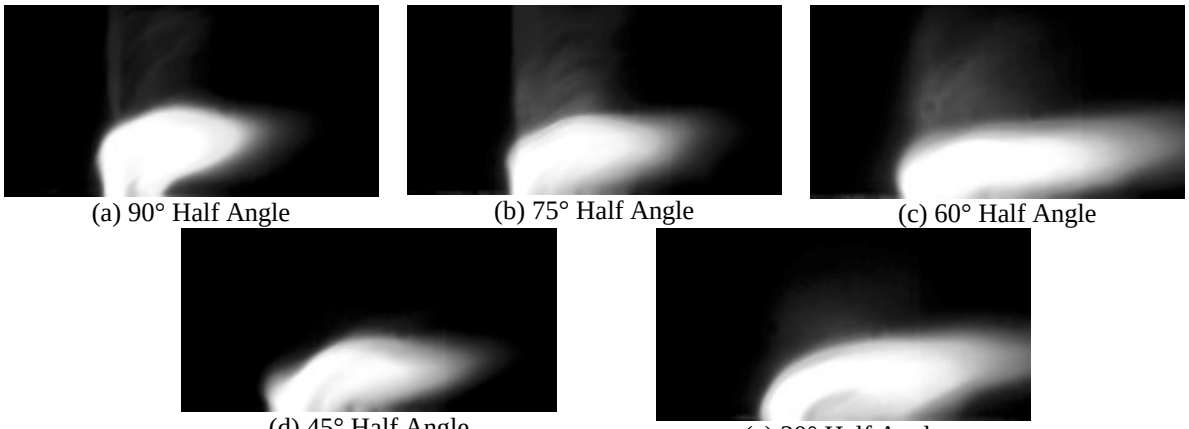

(a) 90° Half Angle (b) 75° Half Angle (c) 60° Half Angle

(d) 45° Half Angle (e) 30° Half Angle

Figure 6.4: High-speed Photographs of Torch Operation in a Mach 3.0 Crossflow

Finally, surface oil-flow visualization techniques were used to study the effects of the anode diverging section on the local flowfield. Pictures of the oil flows are shown in Figure 6.5 for a Mach number of 3.0, no power, and a momentum flux ratio of 2.0. Flow is from top to bottom. The dark circle outlines the interface of the torch anode (d=2.1cm) and tunnel floor. The pictures demonstrate that the anode geometry strongly influences the shape and size of the separation regions in front and behind the torch exit. The 90° design appears to have the largest separation region as well as the widest bow shock.

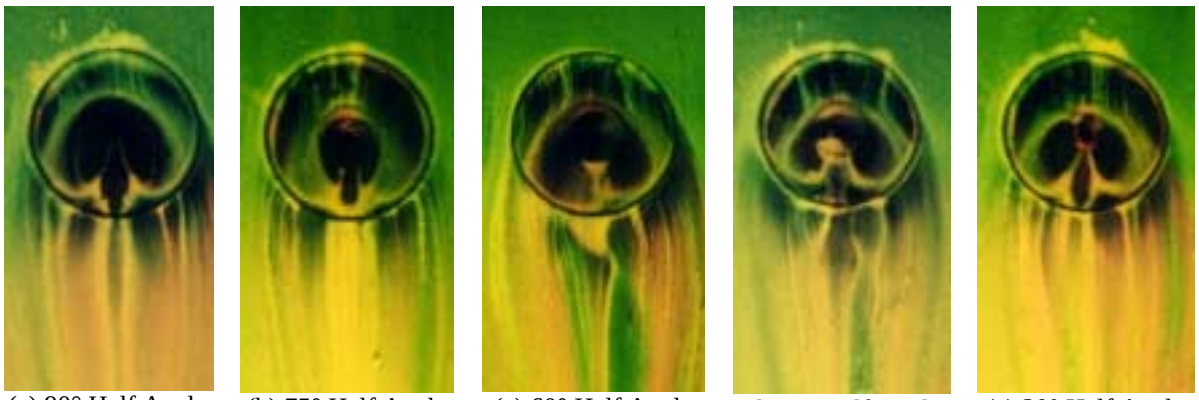

(a) 90° Half Angle (b) 75° Half Angle (c) 60° Half Angle (d) 45° Half Angle (e) 30° Half Angle

Figure 6.5: Surface Oil Flow Photographs of Torch Operation in a Mach 3.0 Crossflow

6.3.2: Geometric Study of Nozzles, Throat Lengths and Injection Angle

This section presents a comparison of the six geometric designs tested (refer to Figure 6.2), followed by subsections discussing specific features of each design. Four types of data are presented: spectral exit profiles, 2D-H_β profiles, total temperature plots, and stereoscopic photographs of the anode surfaces. Procedures for collecting these forms of data were outlined in Chapter 3. Spectral exit profiles are used to determine the stability of a design, whereas the 2D-H_β profiles can be used to qualitatively compare the energy density contained within the plasma. An example of a spectral exit profile for the H_β line is shown in Figure 6.6, and is a representation of the line intensity at various points across the torch exit, located at x=0. Total temperature plots are used to ascertain the penetration height of the thermal energy, and can be used to estimate the mixing effectiveness of such a design. Stereoscopic photographs show arc attachment point locations and whether or not the arc moved during operation.

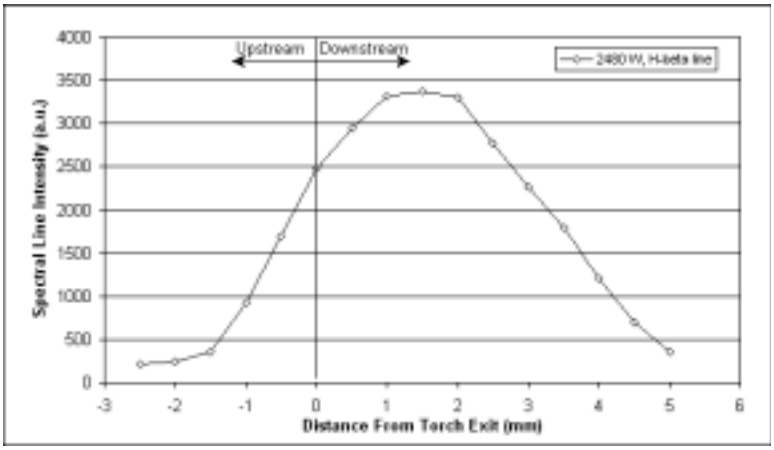

Figure 6.6: An Example of Spectral Exit Profile

In general, it was discovered that 60° designs produced plasmas with higher exit intensities for the H_β line than the corresponding 90° design. Figures 6.7 and 6.8 show the maxima of these exit profiles for each of the six designs, at various powers and a torch momentum flux ratio of 1.17. It is clear that for each sonic design the intensity of the H_β line exhibits a linear dependence on the torch input power. In general, 60° designs had higher slopes than the 90° counterparts, and anodes with longer throat lengths produced higher slopes than anodes with shorter throats.

Through observation of the torch during testing, the slope and x-intercept of these linear trend lines are believed to have significance. The slope of the trend line is thought to be a measure of arc stability, with steeper-sloped designs exhibiting less stability. The two 60°-sonic designs have steeper slopes than the 90°-sonic designs, and suggest that the elliptical exit geometry might be a source of instability because the arc attachment point is fixed at a point where the anode wall is thin and prone to erosion. In addition, long-throated designs were observed to suffer from starting problems, and consequently, also produced exit profiles with larger slopes than short-throated designs.

The x-intercepts of the trend lines indicate the theoretical lowest possible power at which the torch can be operated. Consequently, this intercept corresponds to a zero-radical production rate. Referring to Figure 6.7, the x-intercepts of each design can be determined by extrapolating the linear trend lines. Table 6.2 lists the designs with their corresponding x-intercept. Both Figure 6.7 and Table 6.2 suggest that the 90°-sonic design would be the most stable design, and have the ability to operate at lower power levels than the other five designs. From observation during numerous tests, this was certainly the case. The 90°-sonic design had excellent durability and startability characteristics. Furthermore, 60° designs had higher trend line slopes, and consequently were less stable at lower powers. The 90°-sonic-long design is the only design that does not fit this trend. It had poor starting characteristics and was quite unstable except above 2500 W. The slope of the trend line for this design would indicate that, although less stable than the 90°-sonic design, it would have better stability characteristics than the 60° designs. However, for this particular test series this was not the case.

Table 6.2: X-intercepts for the Six Anode Designs

Anode Design	X-Intercept
90°-sonic	700 W
90°-sonic-long	1000 W
90°-supersonic	1700 W*
60°-sonic	1000 W
60°-sonic-long	1250 W
60°-supersonic	2100 W*

*- Indicates limit of plasma penetration

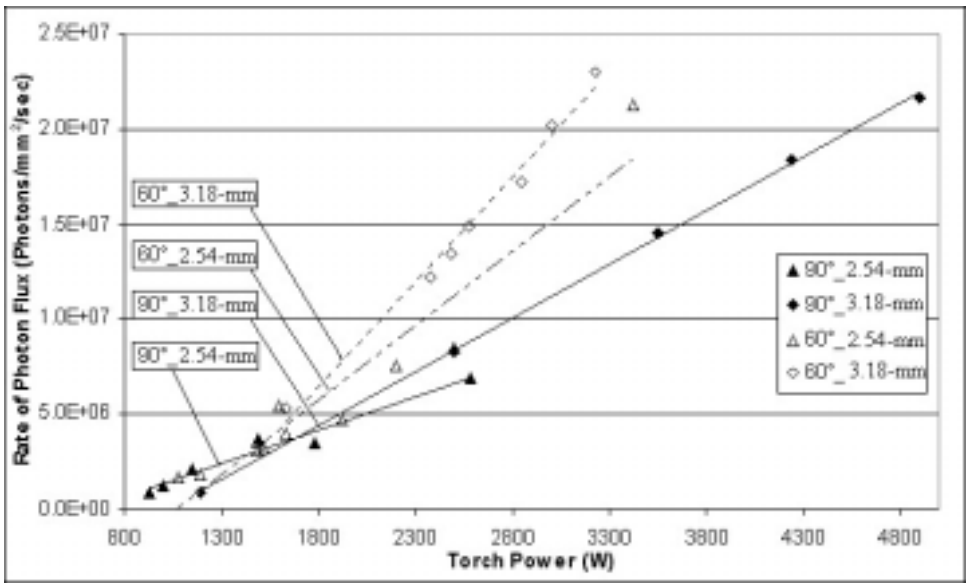

Figure 6.7: Comparison of Exit Profiles for Sonic Designs (H_β Line, q_t=1.17)

The exit H_β line profiles for the two supersonic converging-diverging exit nozzle designs are shown in Figure 6.8. Due to the nature of the design, plasma would penetrate the exit plane of the nozzle only above a certain power. Observation through a welding mask showed that the plasma region was indeed contained wholly within the nozzle for lower powers. However, once the torch power is increased, and the plasma penetrates the nozzle, the characteristic linear trend of power versus spectral intensity is repeated here as with the sonic designs. From the chart, the power at which the plasma penetrated the nozzle for the 60° supersonic design is around 2100 W, while extrapolation of the 90° design suggests plasma penetration would occur at 1700 W, both limits agreeing with observations made during testing. Plasma recombination within the nozzle is essentially wasted energy that could otherwise be used for igniting fuel. In addition, once the plasma does penetrate, the spectral intensity of the H_β line is much lower than for any of the other designs at those powers, indicating that the ignition capability of these designs is inferior to any of the sonic designs. The sonic designs demonstrated that a diverging section is not needed to protect the arc from a crossflow, and the addition of a nozzle actually serves as a detriment to ignition performance by providing a region where plasma recombination occurs, reducing the available energy for igniting fuel-air mixtures. Other methods of evaluation support the conclusion that the 90° designs, generally, perform better than the corresponding 60° designs.

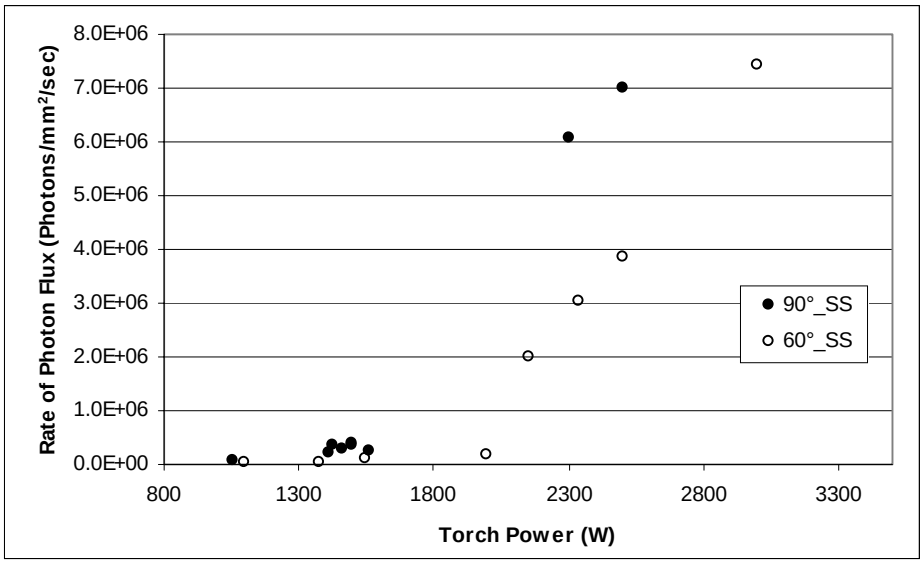

Figure 6.8: Comparison of Exit Profiles for Supersonic Designs (H_β Line, q_{bar}=1.17)

Downstream total temperature measurements were used to measure the penetration height of the thermal energy from the plasma jet, and provided a means to compare the energy content of the gas from one test condition to another. Figure 6.9 presents centerline total temperature measurements for four of the designs at 1500 and 2500 W. The profiles of the sonic-long designs have been omitted for clarity, but are included in sections 6.3.2.2 and 6.3.2.5. From the two charts, several trends can be identified. The first trend is that the two 90° designs have higher maximum total temperature ratios than the 60° designs, indicating the 90° designs may impart more thermal energy to the feedstock gas. As will be shown in the following subsections, this agrees well with the two-dimensional spectral data taken of the plasma jets. In addition, the penetration heights of the 90° designs are higher than the 60° designs, which indicates that normal injection may increase the ignition potential of a plasma torch design by increasing the effective distance at which the jet interacts with fuel molecules.

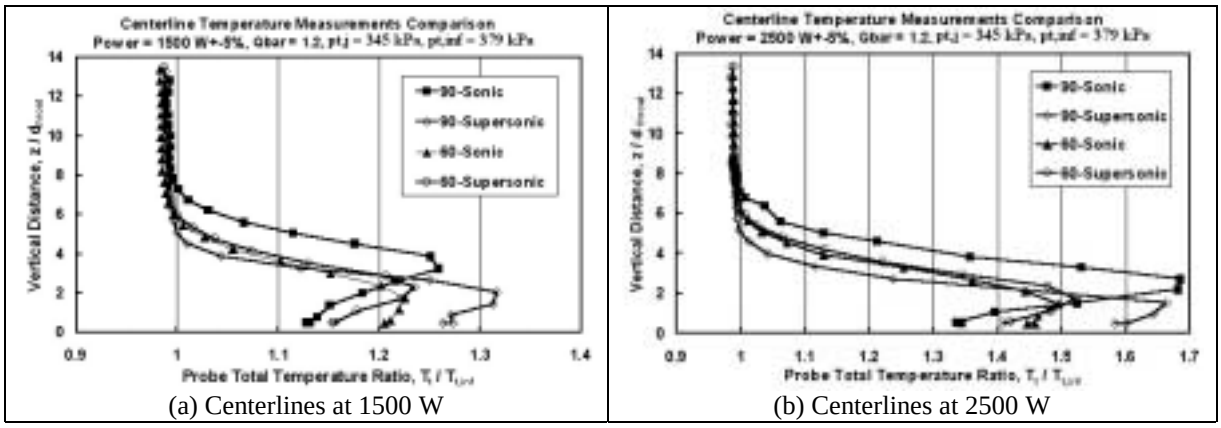

(a) Centerlines at 1500 W (b) Centerlines at 2500 W

Figure 6.9: Centerline Temperature Profiles Comparing Power

The maxima of the profiles presented in Figure 6.9, are plotted in Figure 6.10, along with the maxima of other profiles at different powers. For each of the six designs, it appears that the maximum total temperature exhibits a linear dependence on the torch input power. All designs produce near equal slopes, but the offset of the lines is due to the geometry of the anode. The 90° designs all produce higher maxima than the 60° designs, indicating a larger amount of input energy to the feedstock gas. The measurement of these maxima could be used as a qualitative indication of torch efficiency when calorimeters are unavailable. In addition, the designs tend to cluster together as a function of the injection angle. Both 60° and 90° designs, respectively, perform quite similarly, producing nearly equivalent maximum total temperature ratios throughout the power range of interest. Unexpectedly, the 90°-sonic design produced higher maximum total temperature ratios than the 90°-sonic-long design, the opposite trend experienced with the 60° designs. This could be attributed to the poor stability of the design, or the possibility that the measurements were taken off the centerline of the temperature plume. The latter is more feasible as the centerline was observed to change location occasionally. Regardless, the maximum total temperature ratios measured with the 90°-sonic-long design are still higher than any of the 60° designs, which fit the trend.

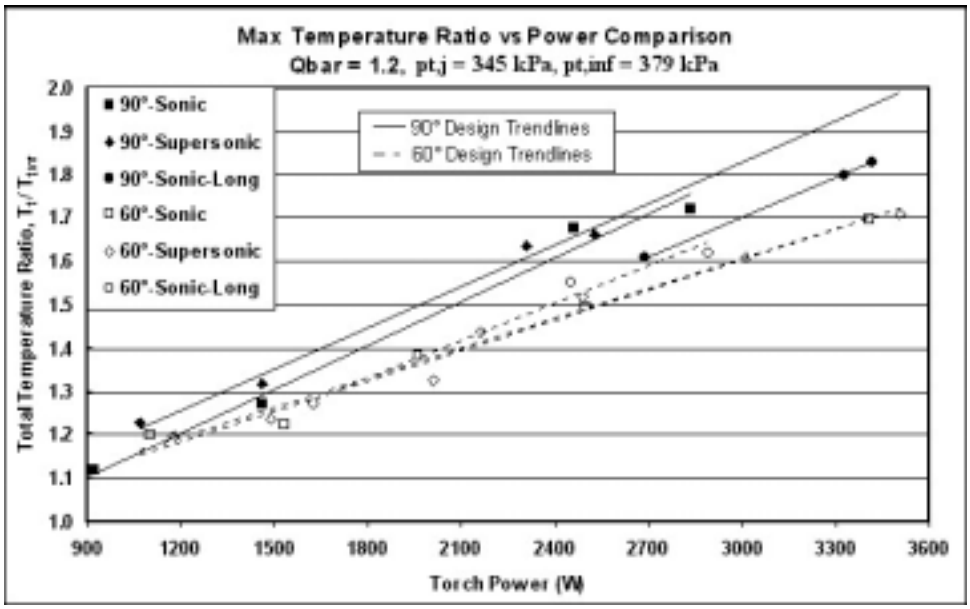

Figure 6.10: Plot of Maximum Total Temperature Ratio versus Power

In addition to the maximum total temperature ratio being dependent on the torch power, the penetration height of each design was also affected by the input power of the torch. Here, the penetration height is defined as the distance above the tunnel floor at which the maximum total temperature ratio occurs. Figure 6.11 shows the penetration characteristics for four of the six designs, comparing the two short-throat sonic designs to the supersonic designs. The penetration heights of the sonic-long designs are slightly better than the short-throat counterparts, but have been omitted so as to improve the clarity of the chart. For all designs, the penetration height of the plume core decreases with increasing power, which may be attributed to a reduction in molecular weight as the dissociation fraction of the feedstock gas increases. The two 60° designs have similar penetration characteristics, but the 60° supersonic design has better penetration over the sonic-short design for the two powers presented here, perhaps as a result of the addition of the nozzle. The difference in performance for the 90° designs is much larger, with the sonic design penetrating two full torch diameters higher than the supersonic design for the power range of interest. The addition of a supersonic nozzle was expected to improve the penetration of the torch plume, but plainly this is not the case for normal plasma injection. The supersonic nozzle on the 90° configuration is clearly a detriment.

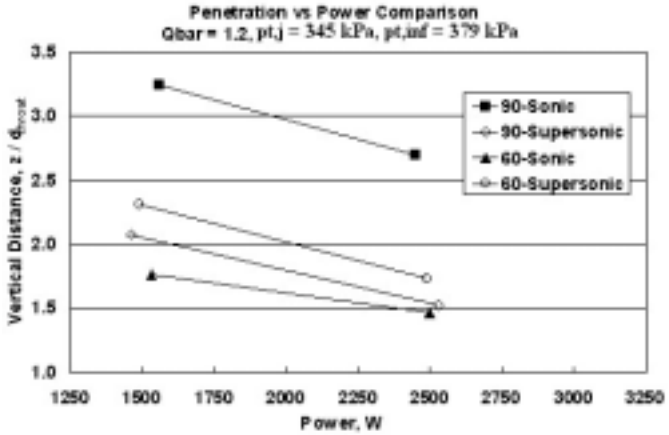

Figure 6.11: Penetration Height versus Power

At this point, a question may arise at the apparent disparity between the spectral exit profiles in Figure 6.7 and the total temperature measurements in Figure 6.10. Why do the 90° designs exhibit lower spectral jet intensities, but higher total temperature ratios? These phenomena seem contradictory, as both are indicative of the energy contained within the feedstock gas, but are actually in sound agreement. This difference is attributed to the geometry of the arc. Arc geometry heavily influences the amount of energy imparted to a feedstock gas, and is a function of the temperature difference between the arc and surrounding gas. The heat, ΔH, carried away from the arc by convection in a cylinder of radius *r* and thickness *dr* is

$$\Delta H = 2\pi r dr \upsilon C_p \rho \Delta T , \tag{6.1}$$

where υ is the uniform velocity of the gas, C_p is the specific heat of the gas, and ρ is the density (Cobine, 1941). A temperature gradient of several thousand degrees per millimeter exists in the gas directly surrounding the arc. Consequently, as the temperature of the surrounding gas approaches that of the arc, the heat transfer to the gas decreases. Furthermore, the temperature of the gas is also a function of the concentration of the ionized atoms within the gas according to the Saha equation

$$\frac{x^2}{1-x^2} p = 3.16x10^{-7} T^{2.5} \varepsilon^{-\frac{eV_i}{kT}} \tag{6.2}$$

where T is the temperature of the gas in Kelvin, and *x* is the fraction of ionized atoms within the gas (Cobine, 1941). From Equations 6.1 and 6.2, it is evident that stationary arcs, producing high local temperatures and ion concentrations, will consequently impart

less overall thermal energy to the feedstock gas because of the lack of arc motion and a lower temperature gradient between the arc and surrounding gases. This concept is illustrated in Figure 6.12. Notice that in the case of the dynamic arc, the maximum temperature near the arc centerline is lower than for the static arc, but the overall bulk temperature is higher.

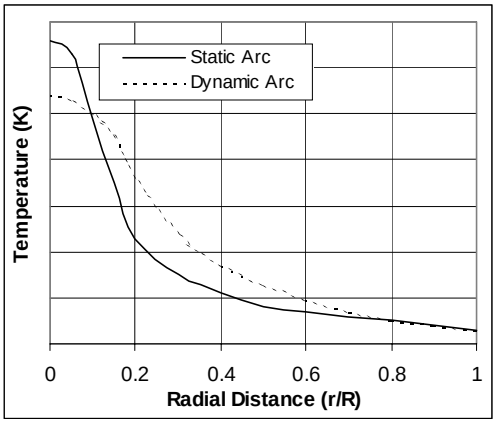

Figure 6.12: Illustration of the Relationship Between Arc Motion and Temperature Distributions

From the present experiments, anodes used for transverse injection, with elliptical exit areas, exhibited less arc movement than did anodes used for normal injection. Assuming the arcs produced with both designs are of equal lengths, the design producing a static arc will create higher centerline temperatures within the constrictor but impart less overall energy to the feedstock gas as a result. Upon exit, these gases will have a higher energy density at the center of the constrictor but have a lower bulk energy density than plasma produced by a dynamic arc. Spectrally, these plasmas will appear brighter at the centerline of the constrictor exit, which was observed. However, after mixing with surrounding gases these plasmas will produce lower total temperature measurements downstream. Comparisons of spectral exit and 2D profiles in the following sections will show that 60° designs do indeed produce higher spectral intensities at the exit, but when integrated over the entire plasma jet, produce a lower average rate of photon flux indicating lower energy density, as would be expected.

6.3.2.1: Results for the 90°, 2.54-mm Throat Length, Sonic Anode

The 90°-sonic design turned out to be the most stable design tested, with a wide operational power range. The performance of this design was consistent from anode to anode, as well as throughout the lifecycle of the anode, producing repeatable results from the first run to the time it was replaced.

Figure 6.13 presents the results from the mass flowrate experiments for methane and the effect mass flowrate has on the H_β line for a range of powers. Here, the mass flowrate is expressed as a momentum flux ratio, for which a conversion can be found in Appendix C. From the chart, the maximum intensity of the H_β line is observed to decrease for higher mass flowrates. This is a combination of two effects, the constriction of the arc, and the increase in thermal mass of the feedstock gas. An increase in thermal mass reduces the temperature rise of the feedstock gas by

$$\dot{Q} = \dot{m} C_p \Delta T \,, \tag{6.3}$$

assuming the heat transfer rate from the arc remains constant. Referring back to Equation 6.2, this will result in a lower ionization concentration and spectral intensity, assuming the arc power remains constant. Furthermore, higher mass flowrates create higher pressures within the constrictor volume, causing the arc to contract. This contraction increases the temperature at the arc core, but reduces the overall diameter of the arc and consequently the area over which heat transfer can occur. The energy imparted to the gas is a function of both the arc radius and temperature, but can be reduced to

$$EI = Ap^m \tag{6.4}$$

where E is the voltage gradient (V/cm), I is the arc current (A), A is a constant, and p is the gas pressure raised to a power of m. The exponent m is always less than one and depends on the gas surrounding the arc (Cobine, 1941). It is clear that an increase in pressure causes the heat transfer to the gas to increase, but this energy transfer is actually a very weak function of pressure and the addition of mass flowrate is much more dominant. As a result, the overall energy density of the gas is reduced, thereby reducing the concentration of excited hydrogen atoms. This trend continues for larger mass flowrates, even though only two flowrates are presented here. The crossing of the trend lines is due to slight intensity variations within the jet with respect to position. It is argued in Section 6.3.2.4 that the lines should be nearly parallel.

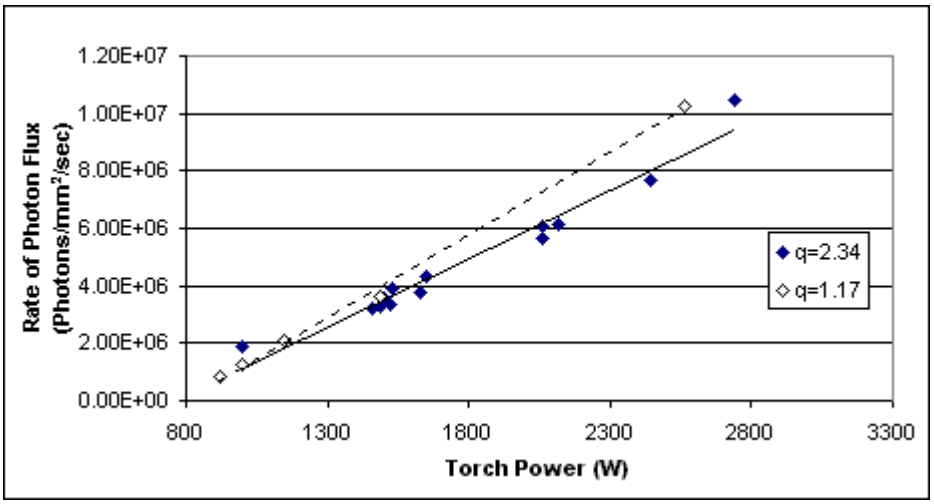

Figure 6.13: Comparison of Exit Profiles for Different Momentum Flux Ratios

Figure 6.14 shows four 2D H_β-line profiles for the 90°-sonic anode. From these figures, the effects of torch power and momentum flux ratio on the plume shape and maximum observed intensity could be determined. These plots identify three important trends: changes in average rate of photon flux within the plasma jet, changes in the maximum rate of photon flux, Ψ, and changes in the penetration height of the spectral plume. The average rate of photon flux is defined as if the total intensity of the region were spread evenly over the described area, in this case, 2 mm upstream, 4.5 mm downstream, and 5 mm above the torch. In addition, the penetration height is defined as the height at which the rate of photon flux within the jet drops below 2.0×10^6 photons/mm^2/sec. This level of photon flux is identified in each plot by a dashed contour. Furthermore, each plot has a unique color scale that corresponds to the rate of photon flux for various points within the plot. The flow is from left to right with the x-position of 0 mm being the center of the torch exit.

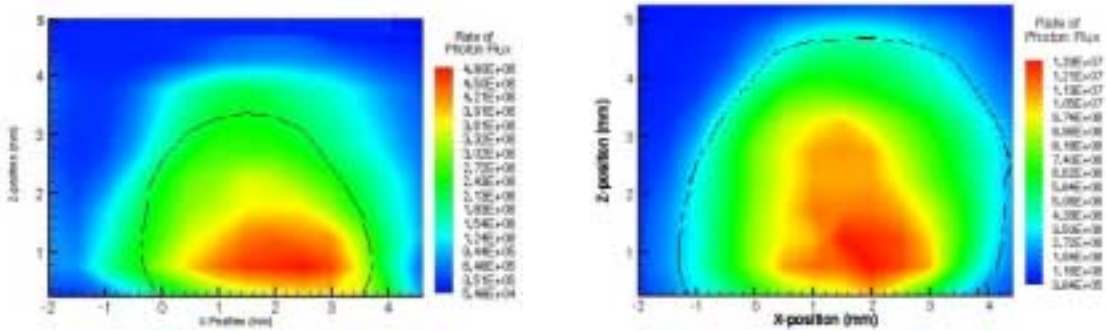

a) 90° Anode, 2.54 mm Throat Length q_{bar}=1.17 1500 W Ψ=1.531x10^6 photons/mm^2/sec

b) 90° Anode, 2.54 mm Throat Length, q_{bar}=1.17, 2500 W Ψ=5.044x10^6 photons/mm^2/sec

c) 90° Anode, 2.54 mm Throat Length, q_{bar}=2.34, 1500 W Ψ=1.405x10^6 photons/mm^2/sec

d) 90° Anode, 2.54 mm Throat Length, q_{bar}=2.34, 2500 W Ψ=3.571x10^6 photons/mm^2/sec

Figure 6.14 2D H_β-Line Profiles for Various Powers and Momentum Flux Ratios

As observed for all the 2D H_β-line profiles shown in Figure 6.13, the spectral maxima occur about 2 mm downstream of the torch exit and slightly above the tunnel floor. This occurs for two reasons. First, the arc attaches on the downstream side of the constrictor, so dissociation due to arc interaction is still occurring for a short distance outside the anode constrictor. Secondly, heat exchange and chemical reactions favor the production of hydrogen atoms within the reaction zone of the plasma jet. The combination of these two effects produces spectral maxima slightly downstream of the torch exit and above the tunnel floor. Recombination occurs shortly thereafter, corresponding to a decrease in the spectral intensity of all species. The shapes of the luminous regions were expected to be toed over due to the strong crossflow. Indeed, observation of the plasma jet through a welding mask verified the jet does toe over, but since hydrogen is such a short lived specie the realization of this is not attained, and the luminous plumes for hydrogen appear as they do in Figure 6.14.

Expectedly, increases in power and decreases in feedstock mass flowrate were both observed to cause an increase in the spectral intensity of the jet. Comparison of 6.14a and 6.14b show that increasing the power from 1500 to 2500 W increases the average rate of photon flux by over 230%. Similarly, for the higher mass flowrate cases, 6.14c and 6.14d, the same increase in power only produces an increase in the average rate of photon flux of 154%. The reason that the higher mass flowrate case shows less increase is due to the addition of thermal mass from the feedstock. Higher flowrates than those presented here would be expected to experience even less increase. In addition, the maximum rates of photon flux increase by 169% for the low-flowrate case, and 238% for the high-flowrate case. This agrees well with earlier trends and is caused by arc constriction. High flowrates, which produce higher constrictor pressures, cause the arc to constrict, thereby increasing the temperature of the arc core and the local production of dissociated species. This is observed through the measurement of higher spectral intensities at the exit of the jet, but as discussed earlier, the increase in thermal mass of the feedstock gas causes a lower mean spectral intensity.

Comparison of the intensity contours in Figure 6.14 shows that only the power, and not the flowrate, affects the penetration height of the hydrogen atoms. Increases in power from 1500 to 2500 W exhibit a 1-mm increase in penetration height for both feedstock flowrate cases from 3.5 mm to 4.5 mm. However, increases in the feedstock flowrate produce no change in the penetration height of the excited hydrogen atoms. In addition, the hot core identified by the red and yellow regions, does not always increase in size or intensity with increasing flowrate. This observation, coupled with the fact that power exhibits only slight influence on the penetration height, indicates that methods to increase the penetration height should be found outside the plasma torch, such as an aeroramp.

Figure 6.15 shows four centerline total temperature profiles, for which the corresponding 2D profiles are shown in Figure 6.16. Four runs are presented here ranging from 900 to 2800 W. As would be expected, increasing the torch power produces a corresponding increase in the maximum measured total temperature, but appears to have little affect on the penetration height. This was not an unexpected trend as the penetration height is only a weak function of the stagnation temperature of the

feedstock gas (Chrans and Collins, 1970). As an item of interest, the 930-W profile was produced during the 55th run of a molybdenum anode, a testimony to the durability of the material.

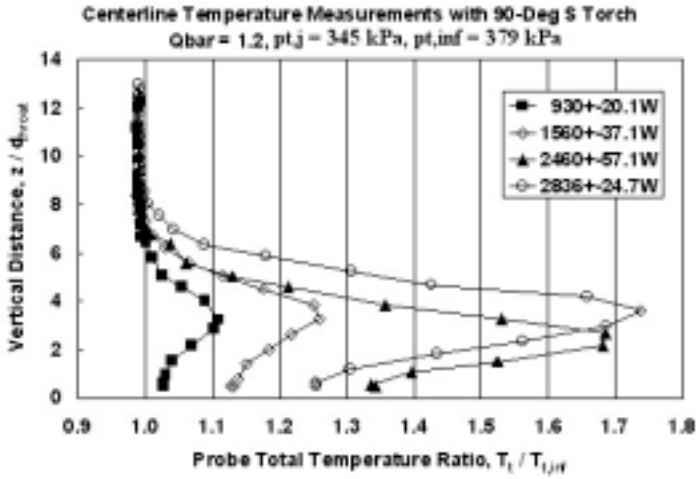

Figure 6.15: Centerline Temperature Measurements for 90°, 2.54-mm Sonic Anode

The 2D temperature profiles shown in Figure 6.16 exhibit several important trends involving the momentum flux ratio of the torch and torch input power. First, the height of the plumes increases with increases in the momentum flux ratio for both the 1500 and 2500-W cases. However, the height of the plume core changes little with input power and for both the 1500 and 2500-W cases. For a momentum flux ratio of 1.17, the height of the core is located about three equivalent diameters, d_{eq}, above the tunnel floor and slightly to the left of the torch centerline. (For a definition of d_{eq} refer to Appendix C.) Increasing the momentum flux ratio to 2.34 increased the penetration height of the core by one full diameter, for both 1500 and 2500 W, and brought the plume fully off the floor.

Increases in the mass flowrate also caused a decrease in the maximum measured total temperature ratios. For 1500 W, Figures 6.16a and 6.16c, doubling the momentum flux ratio decreased the maximum total temperature ratio by 6%, from 1.26 to 1.19. The 2500-W cases also experienced this trend, although the difference was almost three times larger at 16%, a drop from 1.68 to 1.42. This is not to imply that the energy imparted to the feedstock gas by the arc under these conditions is less, but rather the measured value of total temperature is less due to the addition of thermal mass. In fact, the total energy

may even be higher according to Equation 6.4, but the bulk temperature and average spectral intensity are lower due to the added mass.

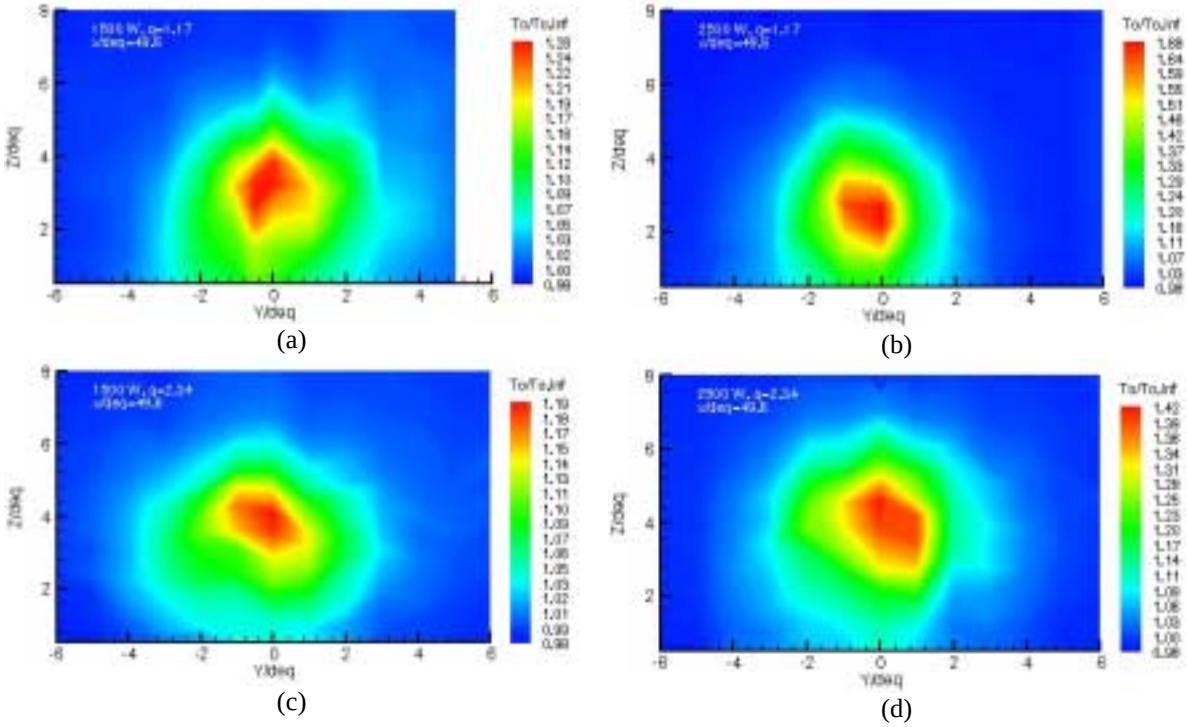

Figure 6.16: 2D Temperature Profiles Comparing Power and Momentum Flux Ratio Variations

Stereoscopic investigation of the 90° short-throat anode after testing confirmed that the arc attachment point was located on the downstream side of the anode constrictor, as shown in Figure 6.17 (flow is from left to right). Molten runoff (1), which was present with other anodes, appears to propagate much further here than in other experiments. A shallow cavity can be seen directly downstream of the constrictor (2), which appears to be the source of the runoff and, because of its size and shape, indicates the arc attachment point was not static during the testing. This cavity is bordered by a shallow buildup of molybdenum (3), which is curved to conform to the outer edge of the cavity. Also two minor cracks are present near the constrictor exit, evidence of thermal loading of the material (4). Finally, a small spire of molybdenum can be seen on the lower edge of the constrictor exit (5), formed by the rapid cooling of the molybdenum by the crossflow.

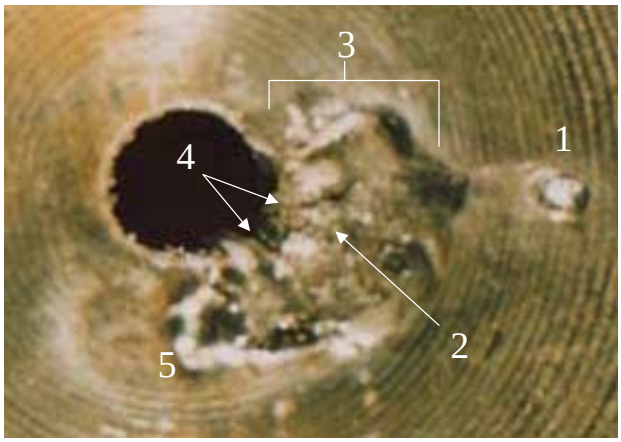

Figure 6.17: Close-up Photograph of 90°, 2.34-mm Throat Length Sonic Anode

6.3.2.2: Results for the 90°, 3.12 mm Throat Length, Sonic Anode

Results for the 90°-sonic-long design are rather sparse because the stability of the design was poor. Of the fourteen total attempted runs with this design, the torch either failed to ignite, or extinguished shortly after ignition in six of them. In addition, after several runs, it was impossible to operate the torch below 1500 W. The cause for this poor operability is the extended throat length, for which a much higher voltage was required to sustain the longer arc column. Since the cathode tips extends partially into the anode constrictor, a 25% increase in the constrictor length from 2.54 to 3.12 mm causes a theoretical increase of 48% in arc length. This increase is substantial and, in this case, caused the operability of the design to be quite poor.

All of the spectroscopic data for this design has been presented in Figure 6.7, where it was shown that the intensity of the H_β line increased linearly with torch power. The remainder of the available temperature data is shown below in Figure 6.18, supplementing the data from Figure 6.10. Only high power cases are available since tests involving lower powers were used to identify the plume centerline and then power had to be increased to ensure operation. Runs from 2700 to 3400 W are shown and, as with the short throat design, the penetration height is affected little by the torch input power. In comparison to the temperature data in Figure 6.11, the penetration height of the 90°-sonic-long design is around three d_{eq}, slightly below the 90°-sonic design, but well above the 90° supersonic design.

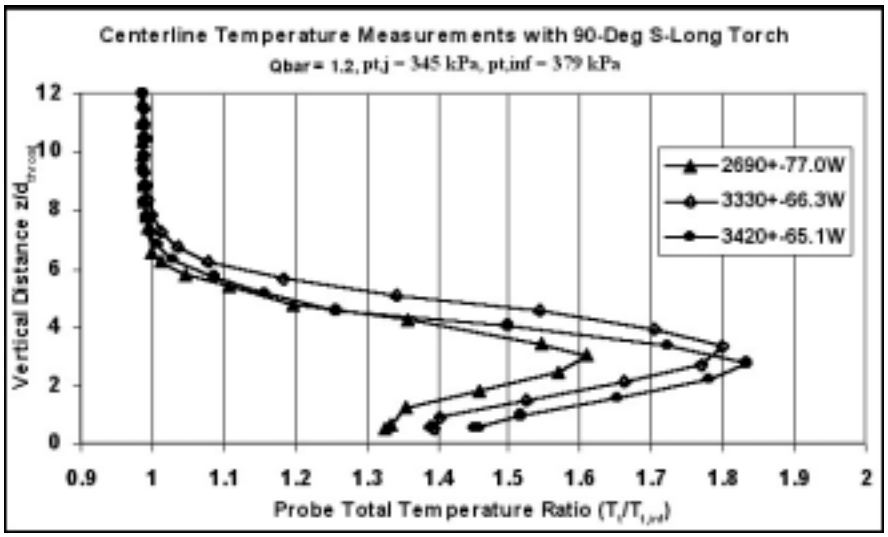

Figure 6.18: Centerline Temperature Measurements for 90°, 3.12-mm Sonic Anode

The stereoscopic investigation of the 90°-sonic-long anode showed features similar to the short-throated counterpart. A close-up photograph of the anode is shown in Figure 6.19 where flow is from left to right and with the line-of-sight originating slightly upstream of the anode exit. As was found to be characteristic with normal injection anodes, the arc attached solely on the downstream side of the constrictor, evidenced by a large once-molten molybdenum bead (1). An area of buildup (2) has been formed directly downstream of this region, creating a separation zone where soot deposits have collected (3). The anode constrictor has been severely eroded on the downstream side, more so than with the short-throat anode even though testing was shorter. This high level of erosion is characterized by deep vertical channels (4), which have been cut away by the arc, and formed as a result of the higher voltage necessary to sustain the arc. Also, two short spires (5 and 6) border the eroded section of the anode throat, and seem to be the center of two regions of light discoloration, characteristic of heat treatment removal. Evidence of heat treatment removal is present downstream of the anode exit (7). Here the heat treatment removal appears to be the cause of heat transfer from the plasma plume due to the plume-like shape of the affected area.

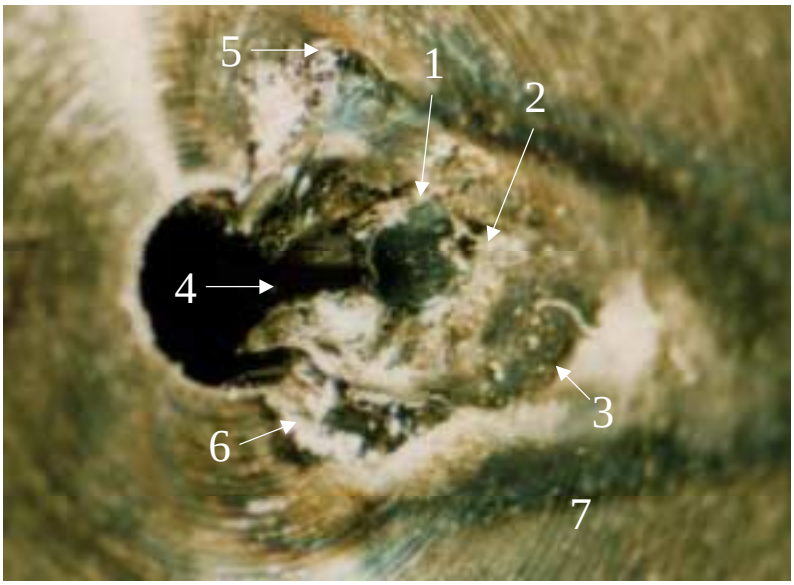

Figure 6.19: Photograph of the 90°, 3.12 mm Throat Length, Sonic Anode

6.3.2.3: Results for the 90°, Supersonic Anode

The addition of a supersonic nozzle to the anode constrictor did not produce the anticipated gains in radical or thermal penetration height. As discussed earlier, the spectrographic data presented in Figure 6.7 showed that the plasma generated within the constrictor did not penetrate the exit plane of the nozzle, except above 1700 W. This essentially nullifies any effectiveness of this design for igniting cross-flowing fuel when operated below this power limit. The temperature data presented is rather limited and reflects the senselessness to fully investigate the performance of this design. However, it should be mentioned that the reliability of this design was good due to the short arc length, and the torch power fluctuated little during the tests as shown by the power fluctuations in the legend of Figure 6.20.

Figure 6.20 shows centerline total temperature profiles for powers ranging from 1000 to 2500 W. As with the other 90° designs, the penetration height is not affected by the torch power, and unfortunately, is not increased through the addition of a supersonic nozzle. It was hoped that the addition of a supersonic nozzle would improve the thermal penetration height over the sonic designs, but it is quite clear that the penetration height of the plume is rather low, just under 2 d_{eq} for all but the 1460-W case. Work in the 1960s by Schetz et al. (1968) demonstrated that a supersonic nozzle does produce some small penetration benefit over a sonic nozzle, but the authors note that, “the only effective

way of changing the penetration of a given amount of fluid through a round hole is by changing the Mach number." In the present case, it appears that the plasma negates, or rather reverses these benefits. According to Rayleigh's theory, a flow, whether subsonic or supersonic, will approach Mach 1 as it is heated. The heating due to the presence of the arc and plasma prevents the nozzle from producing supersonic flow at the exit plane. On a positive note, this design does produce higher total temperature ratios compared to the other two 90° designs. This is likely a result of poor mixing, but may also be attributed to some limited combustion near the nozzle exit where the plasma and heated methane interact with the air stream.

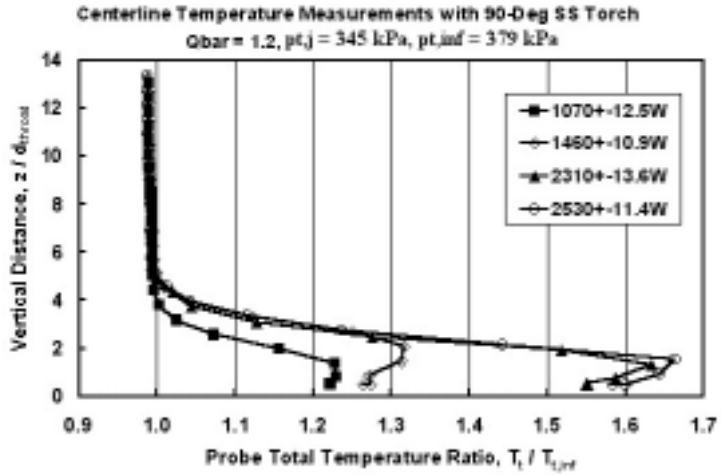

Figure 6.20: Centerline Temperature Measurements for the 90° Supersonic Design

Figure 6.21 shows a 2D total temperature ratio profile, and demonstrates the poor penetration performance of this design. The plume essentially has been trapped on the tunnel floor, with the plume core penetrating just under 2 d_{eq}, and the maximum height of the plume just under 4 d_{eq}. It should be noted that total temperature plumes normally produce symmetric profiles, but in this case a bad set of data at $y/d_{eq} = 3$ causes a peak to occur, which normally would not be present. The core of the plume is oriented along the centerline of the torch indicating that the swirl has had no affect in pushing the plume off to either side. It is clear then, both from the temperature data, and more specifically the spectral data, that the addition of a supersonic diverging nozzle to a normally oriented anode serves only to decrease the amount of energy available for the ignition of fuel. In

addition, the penetration height of this energy is reduced as well, evidenced by the downstream temperature probing.

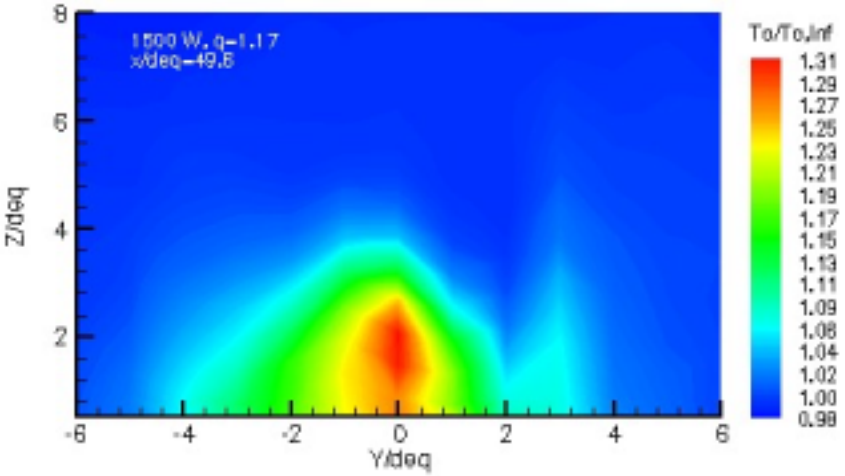

Figure 6.21: 2D Temperature Profile for the 90° Supersonic Design

Two photographs were taken of the 90° supersonic anode after testing and are shown in Figure 6.22, with flow from left to right. Analysis of the anode through the stereoscope showed that quite a bit of erosion of the anode had taken place, producing the broad, uneven flows seen in the nozzle. The pictures are somewhat misleading; the thickness of these flows is rather shallow. However, the important point to mention here is that, in regards to a supersonic nozzle, any amount of erosion destroys the flowfield of the nozzle, negating the purpose for which it was intended. In Figure 6.22a, the angle of view from slightly upstream so that the nozzle and deposits left by the plume can both be seen. The yellow-orange regions downstream of the nozzle (1) are deposits left by the plasma jet and are not caused by heat treatment removal. The center of the plume is white in color mixed with some orange, and then transitions to yellow on the outer edges. It is believed that these deposits are the result of compressor oil from the tunnel compressor being swept downstream into the plasma jet and then burned. Figure 6.22b is a close-up of the nozzle and shows a complex flow pattern of the molybdenum that has been melted and swept through the nozzle (2). The arc attachment point appears to be at the border of the throat and nozzle since the flows originate from this point (3). In addition, the flows have a blackened appearance caused by the close proximity of the methane plasma jet.

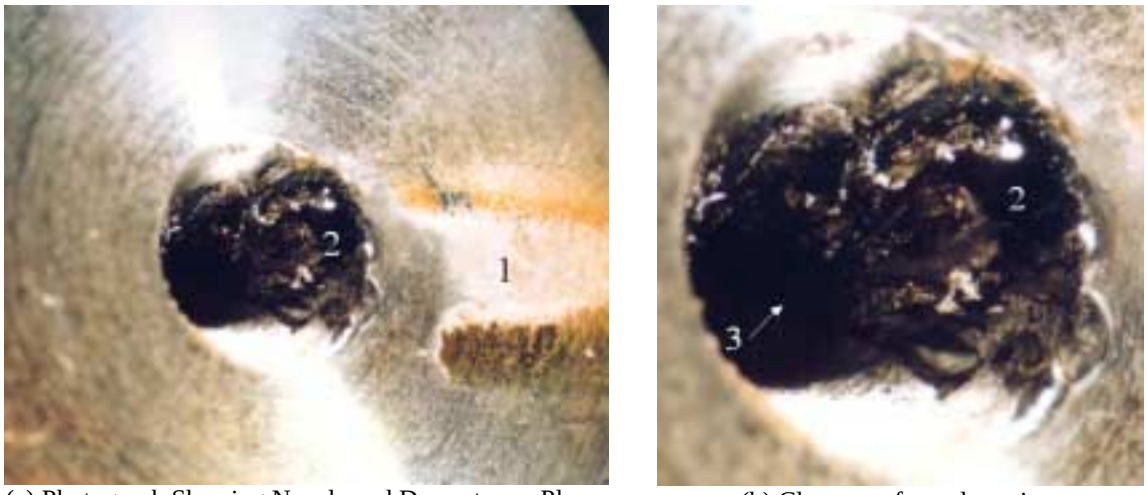

(a) Photograph Showing Nozzle and Downstream Plume Deposits

(b) Close-up of nozzle region

Figure 6.22: Photographs of the 90° Supersonic Anode

6.3.2.4: Results for the 60°, 2.54-mm Throat Length, Sonic Anode

The 60°-sonic design produced repeatable results and exhibited steady performance due to the short constrictor length. Even for tests above 3000 W, torch power varied only slightly from the mean by 1%. The design was easily started for all powers tested. In addition, the erosion rate for the design was slightly higher than for the 90° cases because of the thin region on the upstream side of the constrictor.

Spectrographic evaluation of the 60°-sonic design produced a 2D H_β-line profile with a tilted plume structure. As shown in Figure 6.23, the effect of transverse injection can be seen clearly by the angling of the plasma jet core as well as the outer edges of the region of excited hydrogen. The maximum intensity occurs just downstream of the constrictor exit as expected, but closer to the constrictor exit than for the 90° sonic designs. As discussed earlier, the location of this region is a function of both arc location and the recombination rate of hydrogen. In this case, the arc location has moved slightly upstream as compared to the 90° cases, and the location of this region has moved accordingly. The average rate of photon flux, Ψ, compared to the 90°-sonic design for the same conditions, is 18% lower. This is significant and indicates that for the same power input, this particular geometry produces fewer excited hydrogen atoms. With the goal of using the torch as an igniter, this particular design is inferior based solely on this observation. In addition, the penetration height of the excited hydrogen region is 3.75 mm, slightly lower than the 90° design for the same conditions. Upstream diffusion of

excited hydrogen atoms into the separation zone persists for almost 3 mm, caused by erosion of the thin, upstream portion of the constrictor exit.

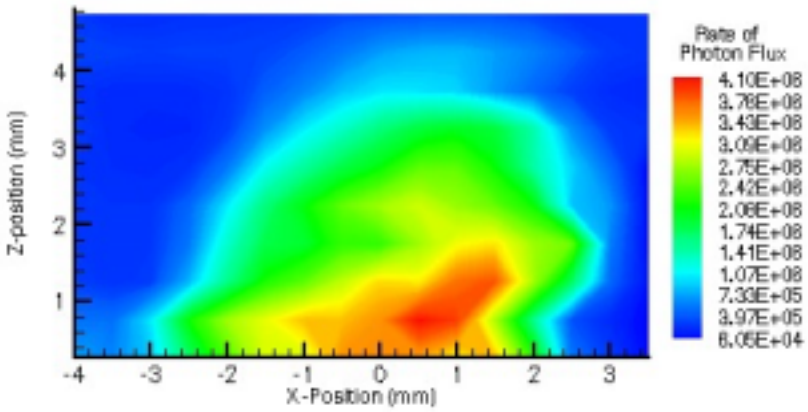

Ψ=1.252x10^6 photons/mm^2/sec

Figure 6.23: 2D H_β-Line Profile for 60°, 2.34-mm Throat Length Anode (q_{bar}=1.17, 1500 W)

Figure 6.24 shows centerline temperature measurements for five runs ranging from 1100 to 3400 W. Although the penetration height of this design was generally poorer than for the 90° designs, this trend worsens for lower powers. The penetration height is well below 1 d_{eq} for the 1100-W case, and increases slightly to 2 d_{eq} for 1530 W. Penetration height for powers above this limit changes little until 3400 W when the penetration height increases slightly to just above 2 d_{eq}.

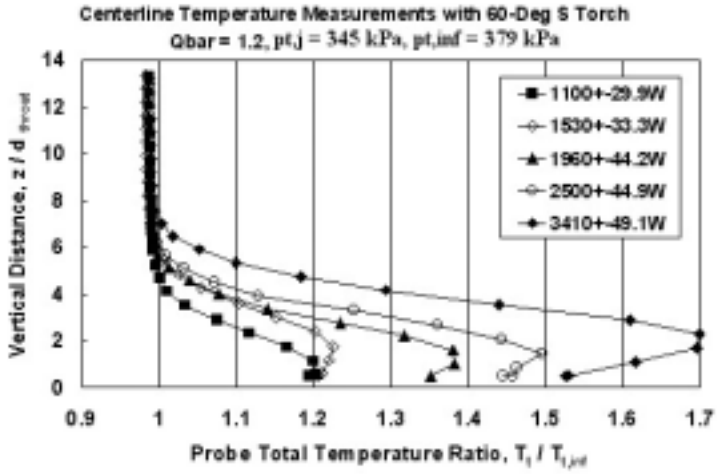

Figure 6.24: Centerline Temperature Measurements for the 60°, 2.54-mm Sonic Anode

A 2D total temperature plot is shown in Figure 6.25 for a torch input power of 1500 W and a momentum flux ratio of 1.17. It is clear from this plot that the thermal

energy produced by the torch is trapped along the tunnel floor. The plume core penetrates to a height of 2 d_{eq}, with the maximum height of the plume reaching just under 5 d_{eq}. Comparison to the 90°-sonic design shows that the penetration characteristics of the 60°-sonic design are much worse, in addition to the maximum total temperature ratio also being slightly lower. Also, the plume core is centered around –0.5 d_{eq} indicating that the swirl has had some effect in rolling the plume off the centerline. It is clear, both from the spectral and temperature data, that for the present purposes the 60°-sonic design is inferior to the 90°-sonic design, in all aspects. It produces plasma with lower concentration of hydrogen atoms, plumes with lower total temperatures, and demonstrates poor mixing and penetration characteristics.

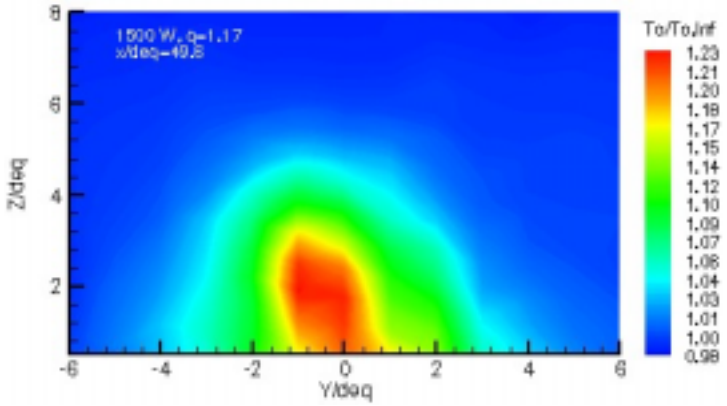

Figure 6.25: 2D Temperature Profile for 60°, 2.54-mm Throat Length Anode

Shown in Figure 6.26 is a photograph of the 60° short-throat anode after testing, where flow is from left to right. Expectedly, arc attachment occurred on the upstream side of the anode exit, evidenced by a deep, curved cavity (1), extending around the upstream portion of the constrictor. As mentioned earlier, the wall thickness of the anode in this region is thin, and therefore is susceptible to high rates of erosion resulting in loss of the flowfield profile. Inside the cavity is a bead of molybdenum (2), indicative of the main arc attachment point, and also a crack (3), evidence of thermal loading. The most interesting structural feature on this anode is the flow that occurred on the upper side of the throat. Here, molybdenum was melted by the arc and then swept downstream (4). At the end of the flow, the molybdenum lifts up off of the anode surface causing a formation like that of paper being blown off of a table (5). More importantly, the size of this flow

more clearly indicates the amount of material removed from the upstream portion of the constrictor.

Figure 6.26: Anode Wear on the 60°, 2.54-mm Throat Length, Sonic Anode

6.3.2.5: Results for the 60°, 3.12 mm Throat Length, Sonic Anode

Despite the increased throat length, the 60°-sonic-long design was quite stable, and did not suffer from starting problems like those experienced with the 90°-sonic-long design. The repeatability and stability of performance allowed in-depth study of the design on a spectroscopic and thermal basis. Spectrographic and temperature measurements were taken for various powers and momentum flux ratios to provide a means of evaluating how the design operated under various conditions.

Spectrographic evaluation of the 60°-sonic-long design showed that increasing the momentum flux ratio of the torch lowered the spectral intensity of the H_β line through the power range of interest. The data shown in Figure 6.27 represent a similar trend as with the 90°-sonic-short design in Figure 6.13, except that the two linear models do not intersect. For a given rate of photon flux, the increased power requirement for the high momentum flux ratio case can be attributed to the constriction of the arc. With the rate of photon flux plotted against current, the trend lines are closer, but still distinctly separate, indicating that the arc geometry also affects the rate of excited hydrogen production. The x-intercept of the trend line corresponds to the point at which radical production is

zero, or more accurately, the theoretical power limit below which torch operation is prohibited with the present power supply configuration. Extrapolation of the trend lines show that the lower momentum flux ratio trend line intersects the x-axis at 1250 W, while for the higher momentum flux ratio, the intercept is 1400 W. For the given flowrates, the torch could not be started below these limits, verifying that spectroscopic analysis of the plasma jet could be used to determine the theoretical limit below which an arc cannot be sustained.

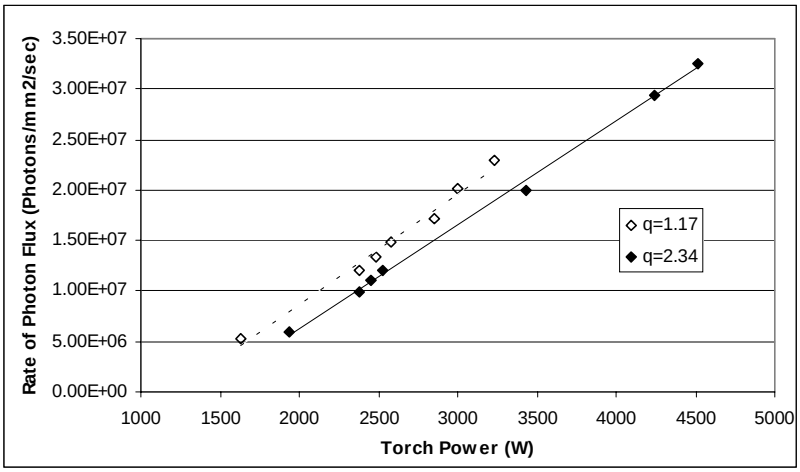

Figure 6.27: Comparison of Exit Profiles for Different Momentum Flux Ratios

Two 2D H_β-line intensity profiles are presented in Figure 6.28 for 2500 W and two momentum flux ratios. The plumes produced for this design exhibit characteristics of both the 60° and 90°-sonic designs. The region of excited hydrogen exhibits much the same overall shape as for the 90°-sonic design, but retains the characteristic tilted core observed with the 60°-sonic design. In addition, the upstream diffusion of excited hydrogen atoms is still evident, caused by the erosion of the upstream portion of the anode constrictor. Also, the region of maximum intensity is still closely oriented to the constrictor exit, caused by the location of the arc attachment point. The increased mass flowrate decreased both the maximum and average rates of photon flux by 18%. As with the spectroscopic studies for the other designs, the penetration height does not seem to be affected by the feedstock flowrate. Only the plume intensity showed dependence on feedstock flowrate.

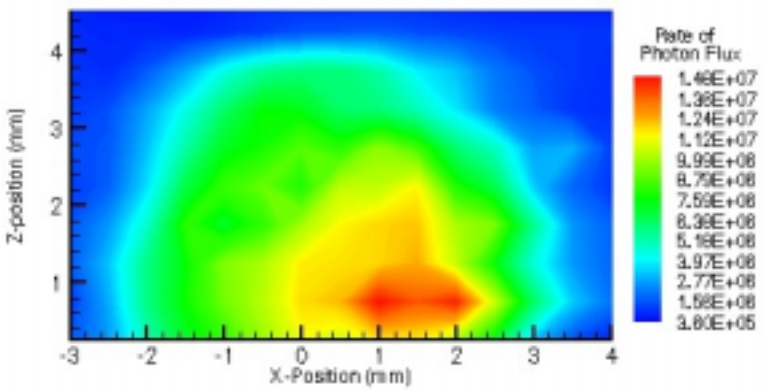

Ψ=4.789x10^6 photons/mm^2/sec

(a) 60° Anode, 3.12-mm Throat Length, q_t=1.17, 2500 W

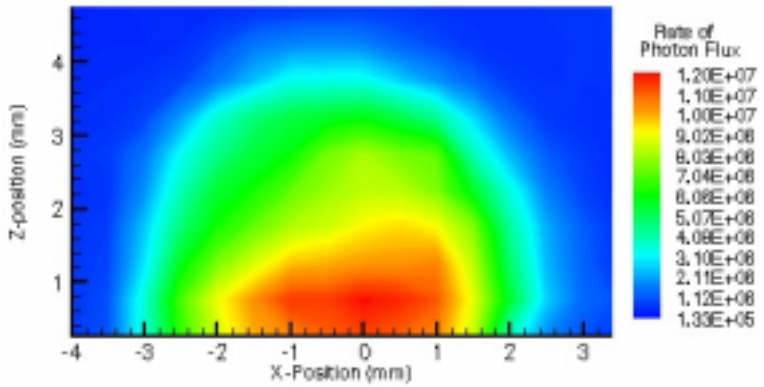

Ψ=3.934x10^6 photons/mm^2/sec

(b) 60° Anode, 3.12-mm Throat Length, q_t=2.34, 2500 W

Figure 6.28: 2D H_β-Line Profiles for Various Momentum Flux Ratios

Total temperature data for the 60°-sonic-long design are presented in Figures 6.29 and 6.30. The centerline data in Figure 6.29 shows similar trends as with other designs, i.e. that power has little influence on the plume penetration height. In addition, increases in torch power produce nearly linear increases in the maximum total temperature ratio. One interesting feature here is the uniformity of the 1500-W profile up to about 3.5 d_{eq}, whereas other profiles exhibit the characteristic peaked shape. This flat profile shape may be an indicator that the design is approaching its lower operational limit of 1250 W, identified by the spectroscopic measurements. A similar profile shape was observed in Figure 6.24 for the 60°-sonic design at 1100 W, with the lower operational limit of that design being 1000 W. If such is the case, total temperature profiles could be used to identify when the performance of a particular geometric design is affected by operating close to the operational power limit.

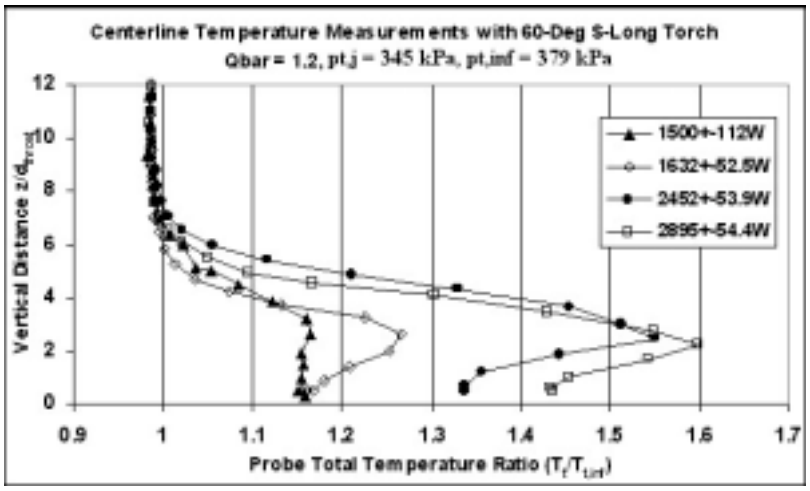

Figure 6.29: Centerline Temperature Measurements for 60° Sonic Long Throat

The 2D temperature profiles in Figure 6.30 demonstrate how changes in momentum flux ratio and torch power affect the downstream plume of the torch. Generally, the temperature profiles produced by this design exhibited good penetration and a symmetric shape, except for the profile shown in Figure 6.30a, where a region of higher temperature gas has formed due to a small flame plume emanating out the side of the torch exit. Increasing the momentum flux ratio of the torch from 1.17 to 2.34 doubled the penetration height of the plume core from 2 d_{eq} to 4 d_{eq}. For the same conditions, the penetration height of the 90°-sonic design was slightly better at 2.5 d_{eq} and 4.5 d_{eq} respectively. Comparison of Figures 6.30a and 6.30b shows a 16% decrease in the maximum total temperature ratio for the higher momentum flux ratio caused by the increase in thermal mass of the feedstock. The swirl of the plasma jet has caused a slight shift of the plume centerline to the left of the centerline of the torch, more so for the lower momentum flux ratio case. Increasing the power from 2500 to 3500 W caused a 35% increase in the maximum total temperature ratio, but did not increase the height of the plume core. In Figure 6.30c, the plume core is directly aligned with the centerline of the torch, but closer inspection reveals that the outer edges of the core extend farther to the left than to the right, evidence that the swirl produced by the torch still has an effect, even at higher powers.

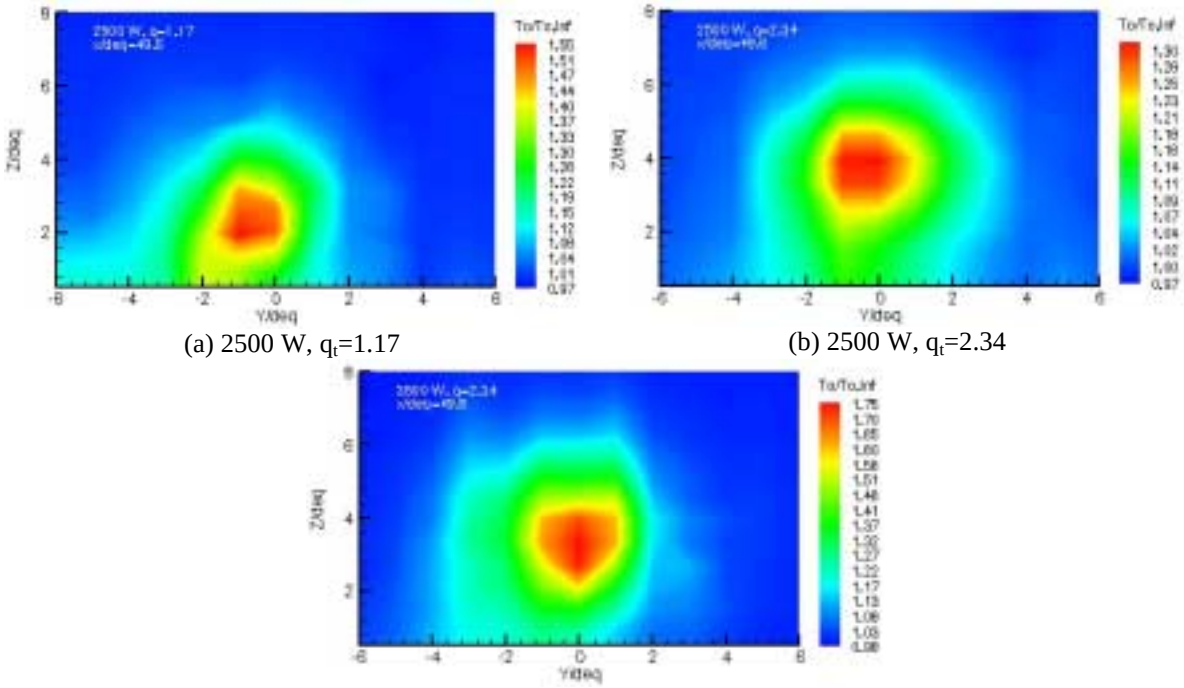

(a) 2500 W, q_t=1.17

(b) 2500 W, q_t=2.34

(c) 3500 W, q_t=2.34

Figure 6.30: 2D Temperature Profiles of the 60°, 3.12-mm, Sonic Throat Anode

Analysis of the anode surface after testing showed that the arc attached on the right side of the anode constrictor, rather than on the upstream side, as was expected. As shown in Figure 6.31, the anode loss (1) is characterized by a deep, narrow channel, cut into the right side of the anode constrictor by the arc. Directly downstream of the channel is a large spire (2) formed from the displaced molybdenum. Also evidence of arc attachment exists on the upstream side of the anode where part of the constrictor has been eroded away (3). A shallow cavity (4) is present adjacent to this region. As with the main cavity on the right side of the constrictor, a small spire has formed downstream (5). In addition to these features, there is also a small, golden-colored bead directly upstream of the anode constrictor (6), which does not seem to be discolored due to heat treatment removal. Finally, a soot trail left by the plasma jet (7), originating mainly from the left side of the constrictor, discolors the anode surface. The swirl induced by the flow swirler, and the presence of the arc on the right side of the constrictor acting as an obstruction, both contributed to pushing the plume out of the left side of the constrictor exit. The downstream evidence of this was shown in Figures 6.28a and 6.28b, where the centerline of the plume is just to the left of the torch exit centerline.

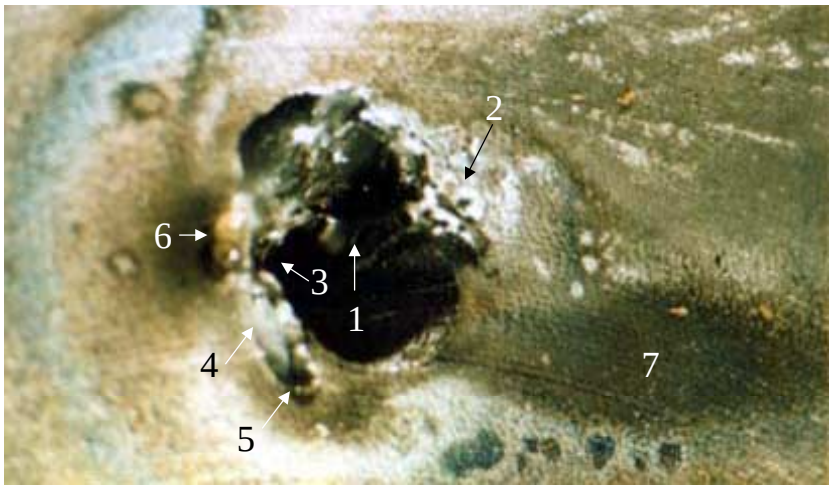

Figure 6.31: Anode Wear on the 60°, 3.12-mm Throat Length, Sonic Anode

6.3.2.6: Results for the 60°, Supersonic Anode

The 60° supersonic design was quite stable and had excellent starting and durability characteristics. All of the spectrographic data for this design were presented in Figure 6.8, and showed that the plasma did not penetrate the nozzle exit plane, except for powers above 1900 W. Essentially, for powers below this limit, a large majority of the energy and excited radicals contained within the plasma jet are unavailable for ignition. The maximum measured temperature ratios were similar to the other two 60° designs, although lower than all of the 90° designs. In addition, the penetration height was not nearly as high as the 60°-sonic-long design, although it was slightly better than the shorter throat version.

A number of centerline temperature measurements were taken for this design across a broad power region, 1200 to 3500 W, and are shown in Figure 6.32. In this case, increases in power show a very slight increase in penetration height, although across the range of interest, the change is so small as to be rather inconsequential. The maximum total temperature ratio increases nearly linearly with torch power, as experienced with all other previous designs.

As shown in Figure 6.33, the plume core penetrates fully off the floor exhibiting a profile very similar to the 90°-sonic design for the same conditions. This is in contrast to the 90° supersonic design, in which the plume core was trapped along the tunnel floor. Comparison to the other two 60° designs shows that the penetration height of the plume is lower than for the long throat design, but higher than the short throat design. As with

the 90° supersonic nozzle, it appears that the nozzle here has little, if any, effect on the penetration height of the feedstock gas. The maximum total temperature ratio here is slightly lower than in the 90° supersonic case, a difference of 1.31 to 1.23, and can probably be attributed the amount of mixing rather than any indication of decreased energy content within the plume. As with the other 60° designs, swirl effects are evident by the slight spread of the plume edge to the left, although the centerline of the plume remains along the centerline of the plasma torch.

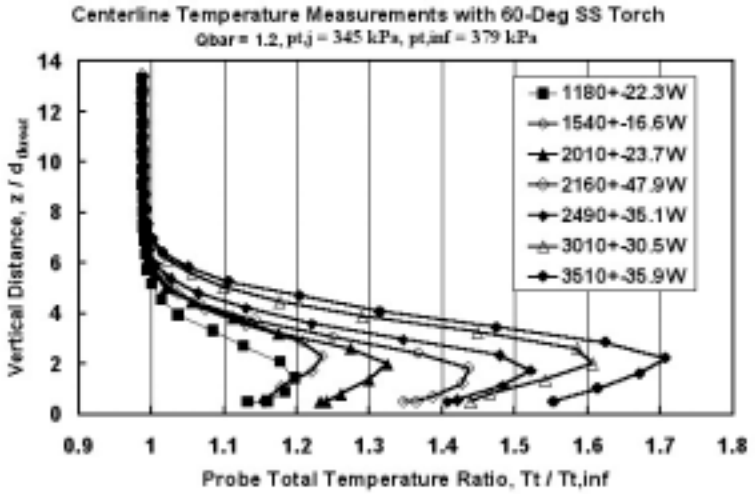

Figure 6.32: Centerline Total Temperature Measurements for the 60° Supersonic Anode

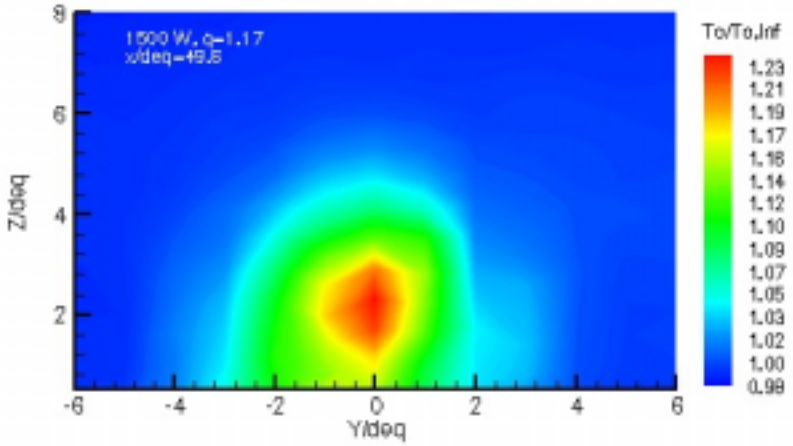

Figure 6.33: 2D Temperature Profile for 60° Supersonic Anode

In comparison to the other stereoscopic investigations, the 60° supersonic anode produced perhaps the most interesting features of all. Figure 6.34a shows the nozzle region and a lightly colored soot trail (1) from the plasma jet, where flow is from left to right. All of the anode wear originates on the downstream side of the anode constrictor,

as evidenced by a large, lustrous flow (2). This flow appears dark because of the viewing angle, and originates at the anode constrictor exit plane. Heat flux from the arc melted the molybdenum near the constrictor exit, which was then pushed up along the surface of the nozzle by convection, forming the flow. The flow lifts off of the nozzle surface near the end of its travel, evidenced by the shadow of the flow (3) on the surface of the nozzle. The volume of the flow appears to be much greater than any present anode wear. Analysis of the interior and exterior anode surfaces showed little surface damage, indicating that this flow may be made up of low-density molybdenum crystals. The formation of this flow certainly affected the penetration characteristics of the nozzle, which was the same problem encountered with the 90° supersonic design. That is, any type of anode wear will cause degradation in the flowfield within the nozzle, negating the purpose for which it was intended. In addition to this feature, there is also some evidence of arc attachment to the left (4) and right (5) of the main flow causing two smaller flows of molybdenum.

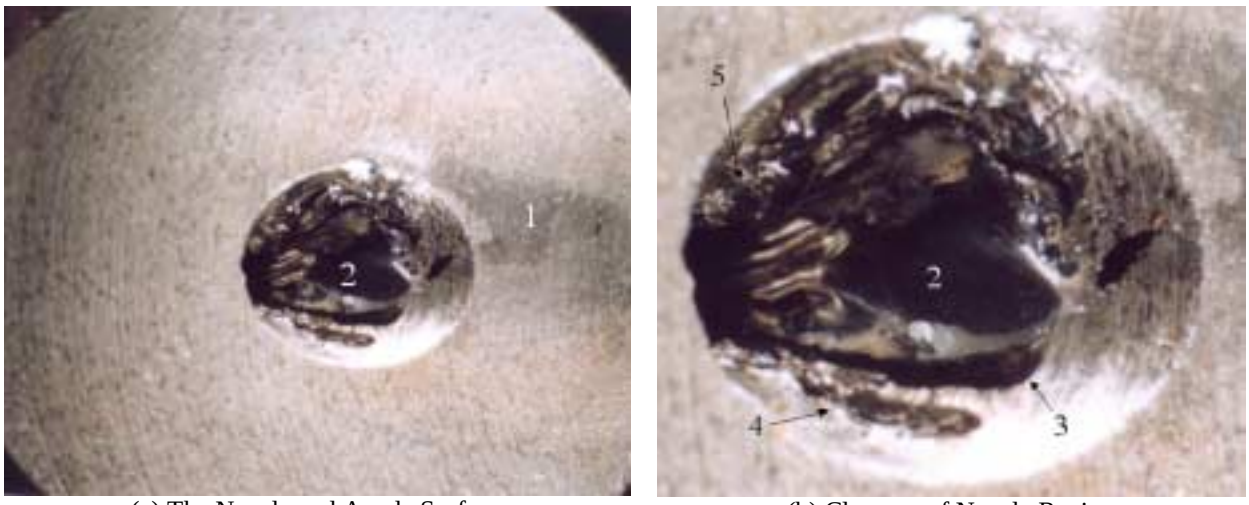

(a) The Nozzle and Anode Surface (b) Close-up of Nozzle Region

Figure 6.34: Close-up Photograph of 60°, Supersonic Anode

6.4: Conclusions

This chapter presented the results of two separate geometric studies of the plasma torch anode, intended to investigate geometric features that could be altered to enhance the ignition capability of a plasma torch. The first study investigated the effects of altering the half-angle of the diverging section of the anode. The purpose of the study was to determine the effect of the half-angle on the power requirements for the torch, and

also to determine if the diverging section was necessary to protect the arc from a supersonic crossflow. For constant current and flowrate, the studies showed that the commonly used half-angle of 45° was the worst design, requiring more power to operate than any of the other four designs. In other applications, this may actually be a benefit, as higher powers can be imparted to an arc for a shorter constrictor length. However, in this application, it is important to maximize the efficiency of the design by reducing the required power input and maintaining the performance. The anode with no diverging section produced lower powers, both for methane and argon feedstocks. This power difference was attributed to a combination of the amount of arc turning, which induces a higher voltage gradient than a straight arc, and an electric field concentration due to the constrictor exit geometry. In addition, supersonic experiments demonstrated that the diverging section was not needed to protect the arc from a supersonic crossflow. Given these two observations, it was concluded that for igniting a cross-flowing fuel-air mixture, the diverging section should be removed, both because of the lower power requirements of the design, and the elimination of the region inside the diverging section where recombination occurs, which essentially wastes the energy otherwise available for ignition.

The second study investigated the effects of throat length, injection angle, and the addition of supersonic nozzles to the anode constrictor. These tests were conducted in a Mach 2.4 crossflow with methane as the feedstock. Spectrographic and total temperature measurements were used to evaluate the performance of each design, while stereoscopic investigations were used to assess the erosion characteristics of the different geometries. In general, increasing the throat length increased the maximum total temperature of the downstream plume, and the intensity of the H_β-line profiles due to the longer arc length. However, in the case of the 90° design, the longer throat length was observed to severely affect the stability of the design. The addition of supersonic nozzles were expected to increase the penetration height of the design, but in actuality hampered the performance of the torch by providing a region in which the plasma could recombine without interacting with the fuel. Only above 1800 W was the plasma observed to penetrate the exit plane of the nozzle, and even then, the intensity of radiation emitted by the excited hydrogen atoms within the jet was much lower than for any of the other designs. In

addition, the anticipated penetration benefits were never realized since the flowfield within the nozzle was disrupted by anode erosion. Finally, the injection angle was found to have a strong influence on penetration height, downstream maximum total temperature measurements, and the intensity of the H_β-line intensity profiles. Anodes designed for transverse injection produced jets with lower overall intensities for excited hydrogen, and plumes with lower total temperature. Although neither method can be used to quantitatively ascertain the energy content within the plasma, the combination of these two effects can imply that the energy imparted to the feedstock gas is less with an anode designed for transverse injection. This was attributed to the stationary nature of the arc, which in almost all cases, attached on the upstream portion of the anode constrictor.

Finally, it was theorized that spectrographic methods could be used to evaluate the stability and lower operational limit of different anode designs. Exit H_β-line profiles showed that the increase in the intensity of the H_β line was linearly proportional to the torch input power. The slope of this function is thought to be an indicator of stability, with lower slopes indicating a more stable design. Observation of the torch during testing supports this theory. The x-intercept, where the linear trend line intersects the power axis, indicates the point at which radical production is zero, and theoretically, the point at which operation of the torch below this limit is impossible. Given the power supply configuration, the designs were incapable of operating below these theoretical limits, substantiating the theory.

In general, these studies were vital for providing a fundamental understanding of how changes in the anode geometry affect torch performance, but also to provide a basis for choosing a design for future work. Based on the measurements and observations made during the two-part experimental study of anode geometry, the normal injection, 2.54-mm throat length anode (90°-sonic) was chosen as the design with which to perform all future experiments. This decision was based on the performance of the design compared to the other five on both a spectral and thermal basis. For a given power and feedstock flowrate, the 90°-sonic design exhibited superior penetration characteristics, and produced plasma jets with higher overall spectral intensities for the H_β line. In addition, the design possesses excellent stability characteristics, and can operate over a wide power range.